Expanding Acquisition and Clutter Filter Dimensions for Improved Perfusion Sensitivity

MinWoo Kim, Craig K. Abbey, Jamila Hedhli, Lawrence W. Dobrucki, and Michael F. Insana, *Fellow, IEEE*

***Abstract*— A method is explored for increasing the sensitivity of power-Doppler imaging without contrast enhancement. We acquire 1–10 s of echo signals and arrange it into a 3-D spatiotemporal data array. An eigenfilter developed to preserve all three dimensions of the array yields power estimates for blood flow and perfusion that are well separated from tissue clutter. This method is applied at high frequency (24-MHz pulses) to a murine model of an ischemic hindlimb. We demonstrate enhancements to tissue perfusion maps in normal and ischemic tissues. The method can be applied to data from any ultrasonic instrument that provides beamformed RF echo data.**

***Index Terms*— Adaptive eigenfilters, blood flow, higher order singular-value decomposition (HOSVD), ischemic hindlimb, power Doppler (PD), ultrasound.**

I. Introduction

THE goal of ultrasonic power Doppler (PD) imaging is to display the magnitude of blood perfusion in tissue at each point in a scan plane. PD methods are sensitive to red-blood-cell (RBC) movements, making them useful for assessing ischemia and flow in tortuous vessels. Nonetheless, quantifying slow and weakly scattering intrinsic perfusion signals remains a formidable challenge. The principal challenge is to increase the signal-to-noise + clutter ratio (SNCR), which is addressed by either suppressing noise and clutter components [1]–[3] or augmenting the blood-flow component with contrast agents [4]–[6]. This paper focuses on noncontrast-enhanced approaches to improving PD imaging.

We provide an initial demonstration of a simple echo-acquisition and data filtering strategy that appears to substantially improve SNCR and Doppler-frequency resolution. With some tuning of the filters, we clearly see regions of slower perfusion that are not visible using established PD techniques. The acquired data at each spatial location are arranged to have two temporal dimensions: slow-time sampled on the order of kHz and frame time sampled on the order of Hz. Temporal sampling is adjusted to increase the density of independent samples in the low-frequency Doppler spectrum where the weak perfusion signal is the strongest. We then increase the dimension of the clutter filter to fully exploit the expanded dimensionality of the data, and employ high-frequency pulses to further increase SNCR.

The recorded data array initially has two spatial dimensions (axial and lateral) and two temporal dimensions (slow-time and frame-time). These data are reordered to combine the two spatial axes into one, resulting in a 3-D data array with one spatial and two temporal axes. We describe the information contained within this 3-D data array and a 3-D clutter filter that separates blood components from clutter and noise.

Traditional filters have been employed in the slow-time domain to reduce power at low temporal frequencies where clutter dominates [7]. The resulting perfusion estimates are often averaged over a few spatial locations and/or multiple frames to reduce variance in the estimates. However, under conditions of slow flow, a significant portion of the perfusion signal may fall into the attenuated frequency channels of the clutter filter. This issue is also present for more general eigenfilters that operate on slow-time echo signals [8], [9].

An alternative to 1-D slow-time filters has been to expand the filter dimension to use information from both space and time to isolate the blood signal [1]; 2-D filters are derived from the echo data using singular-value decomposition (SVD). They exploit the spatial coherence of clutter echoes as distinct from the more incoherent flow patterns of perfusion when separating clutter and blood signals. Today, the estimation of SVD-filtered data often takes place along the spatial and slow-time axes. If frame-time data are recorded, they are averaged to stabilize the SVD filter. Higher sampling rates along the slow-time axis can be achieved with plane-wave imaging techniques [3] that facilitate noise averaging when forming SVD filters from the data.

We propose here to extend SVD filters to 3-D data arrays described previously using a higher order SVD (HOSVD) technique [10], [11]. We will show data that suggest this filter facilitates isolation of echo power from slowly moving and spatially disorganized RBC movement. HOSVD filter construction yields one set of basis vectors for each of the

Manuscript received January 6, 2017; accepted June 21, 2017. Date of publication June 26, 2017; date of current version October 6, 2017. *(Corresponding author: MinWoo Kim.)*

M. Kim is with the Department of Electrical and Computer Engineering, University of Illinois at Urbana–Champaign, Urbana, IL 61801 USA (e-mail: mkim180@illinois.edu).

C. K. Abbey is with the Department of Psychological and Brain Sciences, University of California at Santa Barbara, Santa Barbara, CA 93106 USA (e-mail: craig.abbey@psych.ucsb.edu).

J. Hedhli, L. W. Dobrucki, and M. F. Insana are with the Department of Bioengineering, Beckman Institute for Advanced Science and Technology, University of Illinois at Urbana–Champaign, Urbana, IL 61801 USA (e-mail: hedhli2@illinois.edu; dobrucki@illinois.edu; mfi@illinois.edu).

Digital Object Identifier 10.1109/TUFFC.2017.2719942

three data dimensions within a region of interest. Retaining all three data dimensions enables the adaptive HOSVD filter to effectively separate signal components. We hypothesize that by analyzing data along the frame-time axis, we can enhance the sensitivity of PD imaging to blood perfusion echo signals. The challenge for users is to find a subspace in the HOSVD core array that isolates perfusing blood signals. Projecting the recorded echo data onto that subspace before computing the signal power at each pixel dramatically increases PD sensitivity to perfusion. The process of filter formation includes signal averaging that improves filter stability. However, we must take care to select spatial regions that include only wide-sense stationary echo data.

To test the feasibility of the approach, these measurement methods are applied to muscle-perfusion imaging of healthy and ischemic mouse hindlimbs. Perfusion in this model of surgically induced ischemia generates spatial patterns of perfusion/ischemia [12] that we track to observe and compare with alternative approaches.

II. Methods

A. Notation

The structure of the data array is central to understanding the method. Arrays are described using the following notation. Scalars are written as lower case letters $(a, b, \ldots)$, column vectors as bold lower case letters $(\mathbf{a}, \mathbf{b}, \ldots)$, matrices as bold capital letters $(\mathbf{A}, \mathbf{B}, \ldots)$, and multidimensional arrays or *tensors*[1] as bold calligraphic capital letters $(\boldsymbol{\mathcal{A}}, \boldsymbol{\mathcal{B}}, \ldots)$. Integers i, i_1, i_2, and i_3 are indices, e.g., the ith element of vector $\mathbf{a}$ is denoted as $a_i = \mathbf{a}[i]$, the (i_1, i_2)th element of matrix $\mathbf{A}$ as $a_{i_1,i_2} = \mathbf{A}[i_1, i_2]$, and the (i_1, i_2, i_3)th element of the third-order tensor $\boldsymbol{\mathcal{A}}$ as $a_{i_1,i_2,i_3} = \boldsymbol{\mathcal{A}}[i_1, i_2, i_3]$.

B. Echo Data Arrays

Doppler-mode acquisition involves the recording of echoes following a series of narrow-band pulse transmissions along one or more scan lines. After each pulse transmission, M echoes are recorded at fast-time sampling interval T (see Fig. 1). Let $\mathbf{x}$ represent the complex envelope of the recorded echo signal, i.e., the demodulated analytic signal [13]. Each element of $M \times 1$ vector $\mathbf{x}$ is a complex number with real and imaginary components given by in-phase and quadrature values. The mth fast-time sample, for $1 \le m \le M$, corresponds to axial depth $z = z_0 + (m-1)cT/2$, where z_0 is the distance between the transducer surface and the beginning of the recorded signal, and c is the compressional wave speed.

For each line of site, echo vectors are recorded N times following each of N pulse transmissions to form a packet of echo data. Pulses are transmitted on the slow-time interval $T' > \text{MT}$, where $1/T'$ is the pulse repetition frequency (PRF). Conventional power and color Doppler acquisitions record a packet of echo data for each of L adjacent lines of site separated laterally by the spatial interval D. All packets for one spatial frame form an $(N \times M \times L)$ array of echo data that we call a *Doppler frame*. This conventional 3-D array represents two spatial dimensions and a slow-time dimension.

K Doppler frames are recorded on the time interval $T'' \gg T'$ to generate the frame-time dimension of a 4-D data array. To measure perfusion, we set $T = 0.042$ μs (24 Msamples/s fast-time sampling rate), $T' = 1$ ms (PRF = 1 kHz), and $T'' = 0.11$ s (frame-repetition frequency = 9 Hz). This 4-D data array is represented by $\tilde{\boldsymbol{\mathcal{X}}} \in \mathbb{C}^{N\times M\times L\times K}$.

The second and the third dimension of $\tilde{\boldsymbol{\mathcal{X}}}$ are associated with axial and lateral spatial domain, respectively, that are not separately analyzed. Therefore, the array is reordered as follows:

$$\boldsymbol{\mathcal{X}} \in \mathbb{C}^{N\times S\times K}, \quad \text{such that } x_{n,s,k} = \tilde{x}_{n,m,l,k} \tag{1}$$

where $s = m + (l-1)M$ and $S = \text{ML}$.

The common assumption is that echo data arise from three independent physical sources: tissue clutter $\boldsymbol{\mathcal{C}}$, blood scattering $\boldsymbol{\mathcal{B}}$, and acquisition noise $\boldsymbol{\mathcal{N}}$. Thus, $\boldsymbol{\mathcal{X}}$ has three components

$$\boldsymbol{\mathcal{X}} = \boldsymbol{\mathcal{C}} + \boldsymbol{\mathcal{B}} + \boldsymbol{\mathcal{N}} \tag{2}$$

where each has size $N \times S \times K$. White acquisition noise ensures that $\boldsymbol{\mathcal{X}}$ is full rank. Finally, $\boldsymbol{\mathcal{B}}$ includes signals from fast arterial flow and slow capillary perfusion.

C. Eigen-Based Filters

For echo data well represented by a zero-mean Gaussian process, the correlation (and covariance) matrix contains all the statistical information for that vector space. Eigenfilters decompose the multidimensional data array using eigenvectors of the correlation matrix. These eigenvectors are orthogonal and uncorrelated, and, under the Gaussian assumption, their eigencomponents are as statistically independent as possible. An eigenvalue divided by the sum of all eigenvalues describes the fraction of variance contributed by that eigenmode.

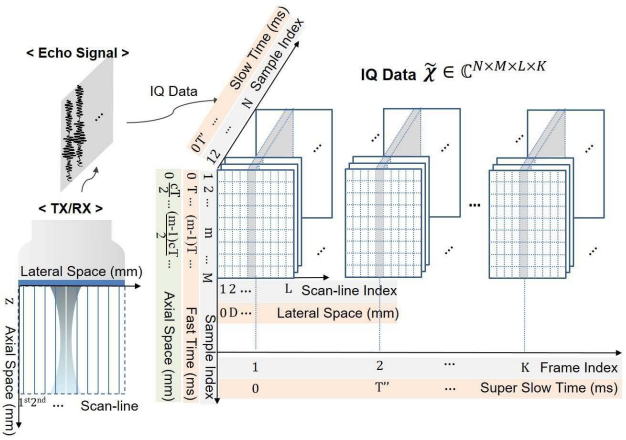

Fig. 1. Data acquisition is illustrated. One IQ echo vector is recorded for each pulse transmission. The fast-time sampling interval is T, generating an $M \times 1$ vector. N echo vectors are recorded with interval T' at each line of site. Repeating the acquisition process over L lateral lines of site with spatial interval D makes one Doppler frame array. Recording K frames at time interval T'' results in the 4-D array of IQ echo data $\tilde{\boldsymbol{\mathcal{X}}} \in \mathbb{C}^{N\times M\times L\times K}$. The array is reformed as a third-order tensor $\boldsymbol{\mathcal{X}} \in \mathbb{C}^{N\times S\times K}$, where $S = \text{ML}$.

[1]We use the term *tensor* to be consistent with the HOSVD literature. However, in our usage, the term does not imply anything about the transformation properties of the multidimensional data arrays.

Because tissue scattering is often more echogenic than blood scattering, and both contribute more to the variance than noise, the common assumption is that clutter dominates the first few eigenvalues, blood the next few, and the rest are noise. Eigen-based filters isolate the blood subspace by identifying the clutter–blood and blood–noise interfaces and suppressing eigenvalues outside the blood subspace [3], [9], [14]. The method used to construct the filter depends on how many of the data dimensions we choose to apply, as we now explain.

1) First-Order Eigen-Based Filter: Let $\mathbf{X} \in \mathbb{C}^{N\times S}$ be a matrix indicating the αth Doppler frame of echo data such that $\mathbf{X} = \boldsymbol{\mathcal{X}}_{i_3=\alpha}$, $\alpha \in \{1, \cdots, K\}$. An empirical correlation matrix of the *temporal signal* can be computed and then decomposed as follows:

$$\mathbf{R}_N = \mathbf{X}\mathbf{X}^\dagger = \mathbf{U}\Lambda\mathbf{U}^\dagger \in \mathbb{C}^{N\times N} \tag{3}$$

where † denotes conjugate transpose. Λ is a diagonal matrix of eigenvalues sorted in descending order. The columns of unitary matrix $\mathbf{U} = [\mathbf{u}_1, \ldots, \mathbf{u}_N]$ are the corresponding eigenvectors for $\mathbf{R}_N$. From (3), $\mathbf{X}$ is easily decomposed in terms of temporal eigenvectors using

$$\mathbf{X} = \mathbf{U}\mathbf{U}^\dagger\mathbf{X} = \sum_{i=1}^{N} \mathbf{u_i}\mathbf{u_i}^\dagger\mathbf{X}\,. \tag{4}$$

Identifying the rank of the clutter and blood subspaces by c and b, respectively, data are processed using the 1-D eigen-based clutter filter

$$\hat{\mathbf{B}} = \sum_{i=c+1}^{c+b} \mathbf{u}_i\mathbf{u}_i^\dagger\mathbf{X}\,. \tag{5}$$

That is, only those eigenvectors associated with the blood subspace are used to resynthesize the decomposed echo data, which is now represented by matrix $\hat{\mathbf{B}}$. Subsequently, the power $\hat{\mathbf{B}}$ is mapped into the PD image.

Note that when the echo signals are wide-sense stationary and the impulse response for the pulse-echo system is linear time-invariant such that the system matrix is well approximated by a circulant matrix, then the eigenfilter components are equal to Fourier components. The difference is that finite-impulse response (FIR) clutter filters are generally fixed over the imaged region while the eigenfilter described in (5) adapts to the echo data.

Similarly, an empirical correlation matrix of the *spatial signal* can be computed and then decomposed using

$$\mathbf{R}_S = \mathbf{X}^\dagger\mathbf{X} = \mathbf{V}\Lambda'\mathbf{V}^\dagger \in \mathbb{C}^{S\times S} \tag{6}$$

where eigenvalue matrix Λ' has a different size but contains the same nontrivial eigenvalues as Λ in (3). The columns of unitary matrix $\mathbf{V} = [\mathbf{v}_1, \ldots, \mathbf{v}_S]$ are eigenvectors in the spatial domain. Equation (6) is not typically used for power estimation although it is an important component of the second-order filters described in the following.

2) Second-Order Eigen-Based Filter: SVD is an analogous tool for decomposing data spanning two vector spaces, in this case, time and space. Matrix $\mathbf{X} \in \mathbb{C}^{N\times S}$ is decomposed using

$$\mathbf{X} = \mathbf{U}\Sigma\mathbf{V}^\dagger = \sum_{i=1}^{r} \sigma_i\mathbf{u}_i\mathbf{v}_i^\dagger\,. \tag{7}$$

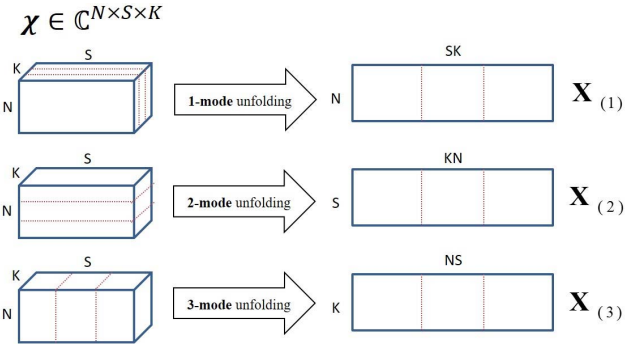

Fig. 2. Figure illustrates 1-, 2-, and 3-mode unfolding operation of the third-order tensor data $\boldsymbol{\mathcal{X}}$.

This form of $\mathbf{X}$ is known as the Casorati matrix [3], whose rows comprise vectorized frames of the image series.[2] Assuming white acquisition noise, the rank of $\mathbf{X}$ is $r = \min(N, S)$, which is also the rank of $\Sigma \in \mathbb{R}^{N\times S}$, a diagonal matrix of singular values σ_i sorted in descending order. Analogous to (5), the best estimation of the blood-signal matrix, in a least-squared sense [3], is found by processing

$$\hat{\mathbf{B}} = \sum_{i=c+1}^{c+b} \sigma_i\mathbf{u_i}\mathbf{v_i}^\dagger = \sum_{i=c+1}^{c+b} \mathbf{u_i}\mathbf{u_i}^\dagger\mathbf{X}\mathbf{v_i}\mathbf{v_i}^\dagger\,. \tag{8}$$

Equations (5) and (8) both seek to identify the blood component of echo-signal variance along the slow-time dimension. N is typically small, which may not provide enough eigenmodes to uniquely identify the blood-scattering subspace given the similarity of perfusion and clutter velocities. Adding frame-time samples increases the number of eigenmodes in a way that also increases the SNCR.

Power contained in filtered data $\hat{\mathbf{B}} \in \mathbb{C}^{N\times S}$ is computed using

$$\mathbf{p}[i_2] = \frac{1}{N}\sum_{i_1=1}^{N} |\hat{\mathbf{B}}[i_1, i_2]|^2 \tag{9}$$

where $\mathbf{p} \in \mathbb{R}^S$ can be converted into an image $\mathbf{P} \in \mathbb{R}^{M\times L}$. Power estimates are log compressed and scan converted when displaying the image for the αth frame acquired.

3) Third-Order Eigen-Based Filter: SVD methods can be extended to 3-D data by decomposing $\boldsymbol{\mathcal{X}} \in \mathbb{C}^{N\times S\times K}$ into three empirical correlation matrices. First, consider the following related to tensor processing.

a) *Unfolding:* A 1-mode unfolding operator $\mathbf{X}_{(1)} = [\boldsymbol{\mathcal{X}}]_1$ arranges elements of tensor $\boldsymbol{\mathcal{X}} \in \mathbb{C}^{N\times S\times K}$ into a matrix $\mathbf{X}_{(1)} \in \mathbb{C}^{N\times SK}$ where columns of the matrix are slow-time signals. Likewise, 2-mode unfolding and 3-mode unfolding generate the matrix $\mathbf{X}_{(2)} \in \mathbb{C}^{S\times \mathrm{KN}}$ and $\mathbf{X}_{(3)} \in \mathbb{C}^{K\times \mathrm{NS}}$ where columns of the matrices are space and frame-time signals, respectively. These are shown in Fig. 2.

[2]Liang [15] showed that the spatiotemporal components of a Casorati matrix are at least partially separable if $\mathbf{X}$ is low rank. With white acquisition noise, $\mathbf{X}$ is always full rank, and yet for echo SNR $\gtrsim$ 20 dB, the rank of the clutter and blood subspaces is much less than the rank of $\mathbf{X}$.

b) *Empirical correlation matrices* are found using the unfoldings as follows:

$$\begin{aligned}\mathbf{R}_N &= [\boldsymbol{\mathcal{X}}]_1[\boldsymbol{\mathcal{X}}]_1^\dagger = \mathbf{U}\Lambda_N\mathbf{U}^\dagger \in \mathbb{C}^{N\times N}\\ \mathbf{R}_S &= [\boldsymbol{\mathcal{X}}]_2[\boldsymbol{\mathcal{X}}]_2^\dagger = \mathbf{V}\Lambda_S\mathbf{V}^\dagger \in \mathbb{C}^{S\times S}\\ \mathbf{R}_K &= [\boldsymbol{\mathcal{X}}]_3[\boldsymbol{\mathcal{X}}]_3^\dagger = \mathbf{W}\Lambda_K\mathbf{W}^\dagger \in \mathbb{C}^{K\times K}\ . \end{aligned} \quad (10)$$

Subscripts on the correlation matrices indicate the $\boldsymbol{\mathcal{X}}$ dimension preserved. Λ_N, Λ_S, and Λ_K are diagonal eigenvalue matrices for the three modes, and $\mathbf{U}$, $\mathbf{V}$, and $\mathbf{W}$ are the corresponding eigenvector matrices.

c) *n-mode rank* of tensor $\boldsymbol{\mathcal{X}}$ equals the rank of the matrix generated by n-mode unfolding

$$r_n\ (\boldsymbol{\mathcal{X}}) = r([\boldsymbol{\mathcal{X}}]_n),\quad n \in \{1,2,3\}\ . \quad (11)$$

Thus, the 1-mode, 2-mode, and 3-mode ranks of $\boldsymbol{\mathcal{X}}$ are the same as the rank of $\mathbf{R}_N$, $\mathbf{R}_S$, and $\mathbf{R}_K$.

Analogous to (7), the HOSVD of $\boldsymbol{\mathcal{X}}$ is

$$\begin{aligned}\boldsymbol{\mathcal{X}} &= \boldsymbol{\mathcal{G}} \times_1 \mathbf{U} \times_2 \mathbf{V} \times_3 \mathbf{W}\\ &= \sum_{i_1=1}^{r_1}\sum_{i_2=1}^{r_2}\sum_{i_3=1}^{r_3} g_{i_1,i_2,i_3}\mathbf{u}_{i_1} \times \mathbf{v}_{i_2} \times \mathbf{w}_{i_3}\end{aligned} \quad (12)$$

where $\times$ denotes an outer-product operation. See the Appendix for an element-based description of the outer products.

$\boldsymbol{\mathcal{G}} \in \mathbb{C}^{N\times S\times K}$ is a "core tensor" analogous to matrix Σ in (7). The columns of $\mathbf{U}$, $\mathbf{V}$, and $\mathbf{W}$ are the eigenvectors for the slow-time, spatial, and frame-time dimensions, respectively. Also r_1, r_2, and r_3 are the n-mode ranks of $\boldsymbol{\mathcal{G}}$. $\boldsymbol{\mathcal{G}}$ is computed using the unitary property of eigenvector matrices

$$\boldsymbol{\mathcal{G}} = \boldsymbol{\mathcal{X}} \times_1 \mathbf{U}^\dagger \times_2 \mathbf{V}^\dagger \times_3 \mathbf{W}^\dagger\ . \quad (13)$$

Components of $\boldsymbol{\mathcal{G}}$ are orthogonal in that the dot product between planes in the array

$$< \boldsymbol{\mathcal{G}}_{i_n=\alpha}, \boldsymbol{\mathcal{G}}_{i_n=\beta} >= 0,\quad \alpha \neq \beta,\ \forall n,\ \forall\alpha,\ \forall\beta \quad (14)$$

and the squared norm of matrix $||\boldsymbol{\mathcal{G}}_{i_n=j}||^2$ equals a jth largest eigenvalue of $\mathbf{R}_n$ for $n = 1, 2, 3$.

HOSVD filtering is analogous to that described for SVD filtering in (8). However, note that the 1-, 2-, and 3-mode ranks of $\boldsymbol{\mathcal{X}}$ are not necessarily the same, and its core tensor $\boldsymbol{\mathcal{G}}$ is not diagonal [10], [11]. Thus, an advantage of HOSVD filtering is the added flexibility in defining the rank of the clutter and blood subspaces.

The HOSVD filter applied to $\boldsymbol{\mathcal{X}}$ (Fig. 3) yields the filtered echo-signal tensor

$$\begin{aligned}\hat{\boldsymbol{\mathcal{B}}} &= \sum_{i_1=c_1+1}^{c_1+b_1}\sum_{i_2=c_2+1}^{c_2+b_2}\sum_{i_3=c_3+1}^{c_3+b_3} g_{i_1,i_2,i_3}\mathbf{u}_{i_1} \times \mathbf{v}_{i_2} \times \mathbf{w}_{i_3}\\ &= \sum_{i_1=c_1+1}^{c_1+b_1}\sum_{i_2=c_2+1}^{c_2+b_2}\sum_{i_3=c_3+1}^{c_3+b_3} \boldsymbol{\mathcal{X}} \times_1 \mathbf{u}_{i_1}\mathbf{u}_{i_1}{}^\dagger\\ &\qquad \times_2 \mathbf{v}_{i_2}\mathbf{v}_{i_2}{}^\dagger \times_3 \mathbf{w}_{i_3}\mathbf{w}_{i_3}{}^\dagger\ .\end{aligned} \quad (15)$$

Constants c_n and b_n are, respectively, the ranks of the clutter and blood subspaces on the ith mode eigenspace. Section IV describes an approach to find 3-D regions within the $\boldsymbol{\mathcal{G}}$ array that best represents the blood components of echo power.

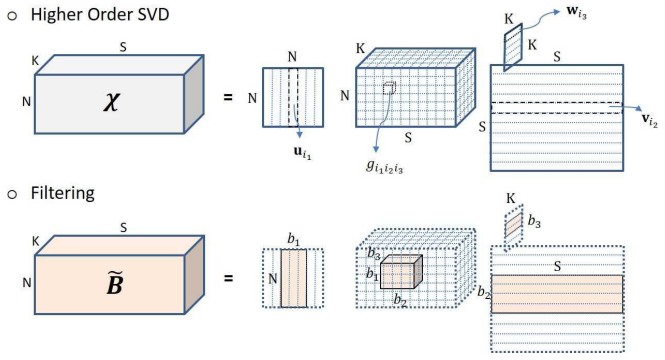

Fig. 3. Top: HOSVD applied to the third-order tensor data $\boldsymbol{\mathcal{X}}$. Bottom: region in the core tensor being selected to isolate the blood-perfusion signal.

TABLE I
ACQUISITION PARAMETERS

Parameter	Value
System	Visualsonics Vevo 2100
Probe type	MS 400
Pulse center frequency	24.0 MHz
Doppler pulse length	2 cycles
Fast-time samples size (Axial length)	200-272 (6.4-8.7 mm)
Fast-time sampling rate	24.0 MHz
Slow-time samples size (Scan time)	17 (0.017 ms)
Slow-time sampling rate	1.0 kHz
Frame-time samples size (Scan time)	100 (11 s)
Frame-time sampling rate	9 Hz
Scan-line numbers (lateral length)	240-250 (14.40-15.00 mm)
Scan-line density	16.67 lines/mm

In contrast with (5) and (8), which were analyzed by others [14], the rank reduction provided by HOSVD filtering in (15) is not optimal in the least-squares sense [16]. That is, the mean-square error between $\boldsymbol{\mathcal{X}}$ and one or more signal components may not be minimized by this filter. Nevertheless, it is a good approximation and can be implemented more simply and quickly than that of iterative methods that can obtain the least-square solution [17].

D. Implementation

We assume that perfusion is constant over the 17 slow-time samples (17 ms) recorded in this paper. However, the echo-signal mean and covariance matrix in the unfolded $\boldsymbol{\mathcal{X}}$ [see (10)], do vary over the 6.4 mm $\times$ 14.4 mm $\rightarrow$ $200\times240 = 48\,000$ spatial samples and over the 17 frame-time samples (1.9 s) typically applied to each PD image. Although we record 100 frames (11.1 s), blocks of 17 frames are applied to any one estimate (see Table I for data acquisition details). Since the number of spatial samples is much larger than either of the time samples, the data are spatially windowed to compute local filters. In this way, an HOSVD filters adapt to the properties of recorded data along any of the array axes.

Beginning with the 4-D array $\dot{\boldsymbol{\mathcal{X}}} \in C^{N\times M\times L\times K}$, spatial window Ω_j of size $N \times \dot{M} \times \dot{L} \times \dot{K}$ is applied J times to $\tilde{\boldsymbol{\mathcal{X}}}$ to make one PD image. Data within the jth window are

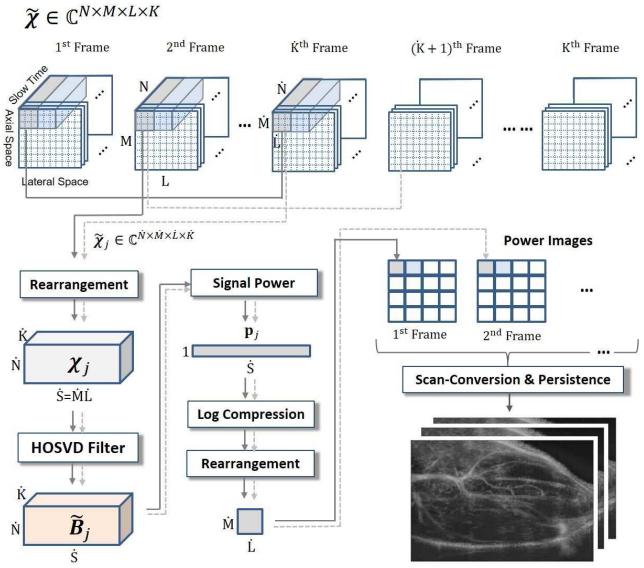

Fig. 4. Sequence of operations leading to the formation of a perfusion image is illustrated. The acquisition data within each window are individually processed. HOSVD filtering isolates the blood-scattering components of the echo signal. Echo power is computed by averaging over slow-time and frame-time axes. The log-compressed power value is assigned a spatial position in the PD image.

rearranged into $\boldsymbol{\mathcal{X}}_j \in \mathbb{C}^{N\times\dot{S}\times\dot{K}} = \mathbb{C}^{17\times224\times17}$, where $\dot{S} = \dot{M}\dot{L}$ for $\dot{M} = 14$ and $\dot{L} = 16$ samples. Each overlaps adjacent windows by 0.13 mm axially and 0.24 mm laterally. A total of $J = 1600$ spatial windows and filters were applied per 6.4 mm × 14.4 mm PD image. We also window data along the frame-time axis if we wish to implement a dynamic sequence of images. Fig. 4 offers a graphical summary.

Similar to (9), the postfiltration signal power within windowed data $\tilde{\boldsymbol{\mathcal{B}}}_j \in \mathbb{C}^{N\times\dot{S}\times\dot{K}}$ is computed using

$$\mathbf{p}_j[i_2] = \frac{1}{N\dot{K}} \sum_{i_1=1}^{N} \sum_{i_3=1}^{\dot{K}} |\tilde{\boldsymbol{\mathcal{B}}}_j[i_1, i_2, i_3]|^2 \tag{16}$$

where $\mathbf{p}_j \in \mathbb{R}^{\dot{S}}$. The elements of vector $\mathbf{p}_j$ are log-compressed and scan converted into a spatial segment of size $\dot{M} \times \dot{L}$. These segments are then assembled into a PD image. Final images may sum sequential PD frames formed along the frame-time axis or display them as a dynamic sequence with adjustable persistence. The latter is preferred if perfusion varies over the acquisition time.

In summary, three eigenanalyses are performed on $\boldsymbol{\mathcal{X}}$ via (10). From the three sets of eigenvectors generated, the core tensor is formed via (13). We then select a region within the core tensor that contains information about perfusion and zero the other elements via (15). This process yields the perfusion subspace whose elements are squared and summed in (16) to estimate the signal power mapped into PD images. *In vivo* experiments in the following show that the perfusion subspace is confined to a small region within $\boldsymbol{\mathcal{G}}$. Therefore, we find it is fast and easy to exhaustively search for values of c_n and b_n in (15) that yield the "best" perfusion maps shown in the results in the following.

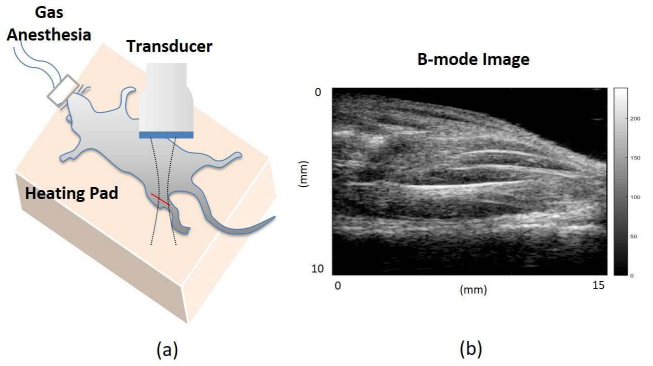

Fig. 5. (a) Anesthetized mouse placed on a heated surface in a supine position is scanned with a linear array. (b) Longitudinal cross section of the hindlimb is displayed as a B-mode image.

Echo data were recorded using a Vevo 2100 system and an MS400 linear array (FUJIFILM VisualSonics Inc., Toronto, ON, Canada). The transducer transmits two-cycle pulses with a 24-MHz center frequency. All processing was implemented in MATLAB 2013b on an Intel processor i5-4300U CPU, 2.50 GHz. The highest computational burden is filter construction, which was performed using a truncation technique [18] to minimize running time. The average time to compute the 1600 windows for one PD image frame is 19.1 s.

E. In Vivo Perfusion Imaging

A murine model of partial hindlimb ischemia was used [19] to study the feasibility of our methods for *in vivo* perfusion imaging (Fig. 5). Each mouse was anesthetized with 1.5% isofluorane vaporized in O_2 at a rate of 1 L/min via nose cone. Each animal underwent hindlimb occlusion of the right femoral artery, following the procedure described previously in [12] and [19] without disturbing nonfemoral peripheral flow to the right leg or any blood flow to the left leg. Briefly, the anesthetized mouse was placed on a 37 °C heating pad, a small incision was made on the right leg to expose the femoral vasculature, and dual ligation of the femoral artery was performed distal to the profundus branch to induce unilateral hindlimb ischemia. To confirm the occlusion and the reduction of blood flow in ischemic hindlimb, animals were imaged with a laser Doppler imager (moorLDI, Moor Instruments, U.K.) before, and immediately after ligation. For the U.S. scanning at 24 h postsurgery, the anesthetized animal was placed in a supine position with hindlimbs extended, and the transducer scanned the shaved inner hindlimb along a longitudinal cross section that included muscle, bone, and vasculature.

Fig. 5(b) displays a B-mode view of the anatomy. Although measurements were made on three mice, we will show the results of scanning contralateral limbs of two mice specifically to compare methods. All experiments were performed with the approval of the Institutional Animal Care and Use Committee of the University of Illinois at Urbana–Champaign following the principles outlined by the American Physiological Society on research animal use.

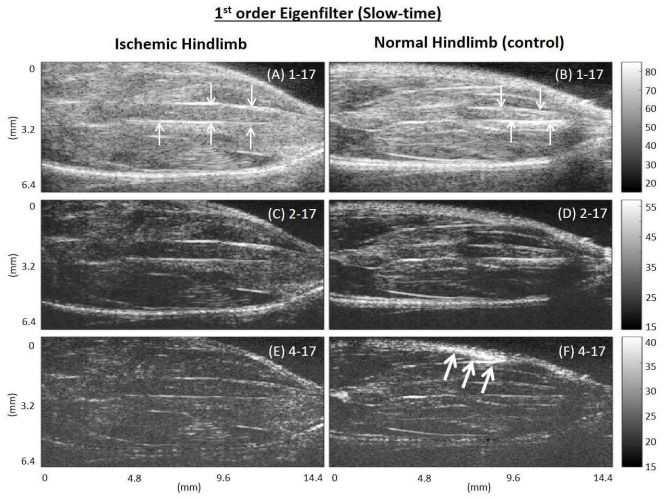

Fig. 6. PD images are shown without a B-mode component. These images are formed using a first-order eigenfilter and slow-time eigenbases. Left and right columns show the images of ischemic and normal hindlimbs, respectively. Thin arrows indicate bone echoes and thick arrows indicate fast arterial flow. The numbers at the top of each image indicate the range of indices passed through the filter in the summation of (5). Since the possible range is 1–17, lower rows are more heavily filtered images.

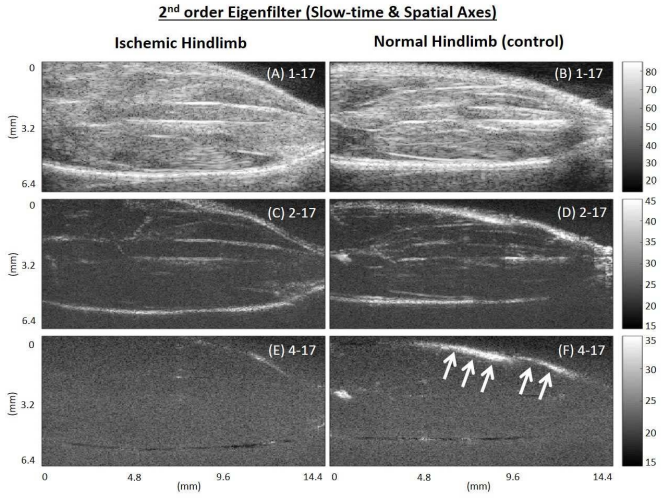

Fig. 7. PD images using a second-order SVD filter based on slow-time and spatial eigenbases to show primarily arterial flow. Left and right columns show the images of ischemic and normal hindlimbs, respectively. Thick arrows indicate a region with fast arterial flow. The numbers at the top of each image indicate the range of indices passed through the filter in the summation of (8). Possible range: 1–17.

III. Results

We recorded 100 sequential Doppler frames (11.1 s) from the right (ischemic) and left (healthy control) hindlimbs one day after right femoral-artery ligation. Only the first 17 frames are included in each of the PD images shown in the following. Images in Figs. 6–10 are from one animal, while in Fig. 11 (left) is from a second animal undergoing identical procedures.

1) First-Order Filter: We begin by processing only the first Doppler frame in the array; specifically, $\mathbf{X} = \boldsymbol{\mathcal{X}}_{i_3=1} \in \mathbb{C}^{17\times 200\cdot 240\times 1}$. Applying the spatial window described in Section II-D, the data matrix used to form the jth spatial window for the first-order eigenfilters was $\mathbf{X}_j \in \mathbb{C}^{17\times 14\cdot 16}$. Computing the temporal correlation matrix in (3) and filtering the data using (5), we constructed the perfusion images found in Fig. 6.

The first row of Fig. 6(A) and (B) displays images obtained without filtering to show the full clutter component in the PD signal. Arrows indicate echoes from bone surfaces. The second row of Fig. 6(C) and (D) shows the filtered images formed by discarding the first (most energetic) slow-time eigencomponent and preserving eigencomponents 2–17. Third row images, Fig. 6(E) and (F), discard the first three slow-time eigencomponents, leaving 4–17. Discarding the three most energetic eigenvalues removes many of the clutter echoes from both images, although the bone reflections remain. More importantly, there is no apparent discriminability between the ischemic and control states except for the appearance of a segment of arterial flow as indicated by the larger arrows in Fig. 6(F) near the proximal skin surface of the control hindlimb.

2) Second-Order Filter: The same data were processed by the second-order SVD filter via (8). Fig. 7 shows the resulting PD images using slow-time and spatial eigenbases.

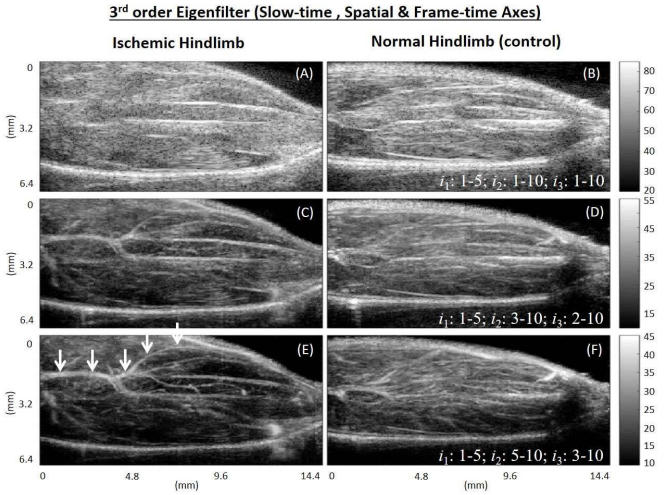

Fig. 8. PD images using the full 3-D data array and HOSVD filter to show perfusion. Left and right columns show the images of ischemic and normal hindlimbs, respectively. Filter parameters shown at the bottom of an image apply to the normal and ischemic images in that row. As filter parameters change, vascular structures emerge [arrows in (E) point to one branch] while clutter and noise components fade. The normal flow image (F) is uniformly perfused, although the signal strength near the bottom surface of the leg is low because of acoustic attenuation. In contrast, the ischemic hindlimb in (E) with lost femoral-arterial flow shows perfusion-deficit patches and prominent vessels that now contain low-speed blood flow from the remaining peripheral vessels. Note that the same echo data are used to form images in Figs. 6–8.

As in Fig. 6, the three rows describe three levels of filtering given by numbers in the upper right corner. Virtually, all echoes are eliminated in the images of Fig. 7(E) and (F) except for the arterial flow near the skin surface in the control hindlimb. Comparing Figs. 6 and 7, we see the effectiveness of including the spatial axis of the data array for clutter suppression. However, the slow-time axis offers very little sensitivity to perfusion signals; the remaining signal power indicates a segment of arterial flow (arrows).

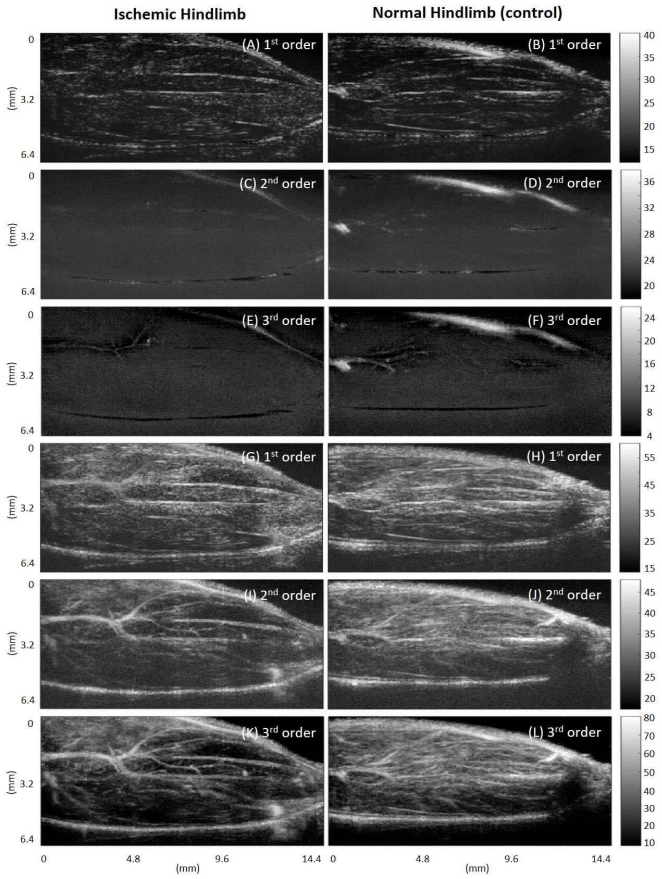

Fig. 9. Comparisons of the visually clearest examples of the first-, second-, and third-order filters applied to the slow-time data axis (A)–(F) to display arterial flow and to the frame-time data axis (G)–(L) to display perfusion. Each image is based on the same 17 frames of echo data.

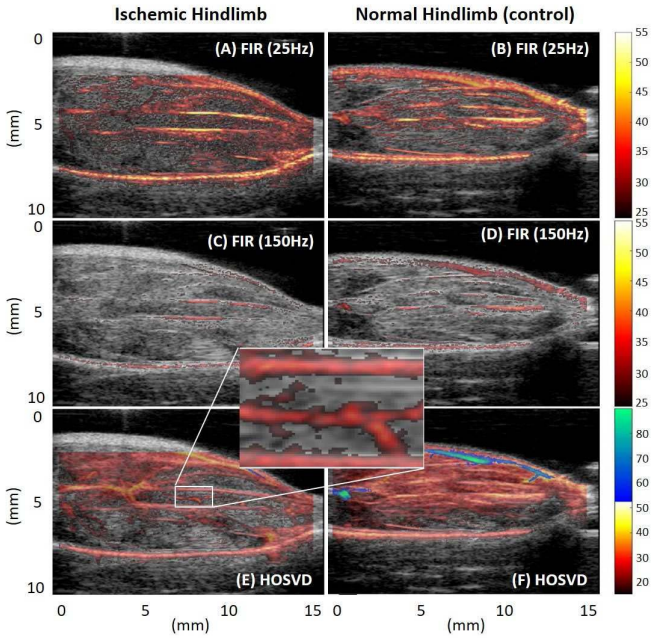

Fig. 10. PD images are compared using standard FIR clutter filtering (first row: 25-Hz high-pass FIR filter and second row: 150-Hz high-pass FIR filter) and adaptive HOSVD filtering (third row) applied to the same data array. Notice that perfusion in the control limb is fairly uniform, except in distal regions where the SNCR is low. Conversely, the ischemic limb shows patchy perfusion throughout. Inset: enlargement of microvessels. Given that the PD pixel dimensions are 32 μm axially and 60 μm laterally, we are resolving 160-μm-dia vessels axially and 300-μm-dia vessels laterally. Axial resolution for 24-MHz pulses with 12-MHz bandwidth is approximately 128 μm. The blue and red colorbars indicate, respectively, color maps related to slow-time power (dB) and frame-time power (dB).

3) Third-Order Filter: We again analyzed the same echo data array but now employing all three dimension using the HOSVD filters of (15). In Fig. 8 (bottom row), we see the emergence of vascular structures that are not at all apparent with 1-D and 2-D filters in Figs. 6 and 7. There are three sets of filter indices, i_1, i_2, and i_3, that specify the ranges in $\mathcal{G}$ passed by the 3-D filter. These are given at the bottom of the images, where values shown apply to both images in that row. Here, we see perfusion and slow vascular flow but very little fast flow or clutter. The advantages brought to bear in these result are threefold. First, the use of frame-time data enhances SNCR for perfusion. Second, employing all three data-array axes increases the effectiveness of clutter filtering. Third, we use more data than that applied to the results of Figs. 6 and 7, which greatly suppresses acquisition noise.

In Fig. 9, we compare the results of the first-, second-, and third-order clutter filters for displaying the slow-time arterial flow (first three rows of images) and frame-time perfusion (last three rows of images). All results are obtained from the same echo-data array, viz., $\boldsymbol{\mathcal{X}} \in \mathbb{C}^{17\times 200\cdot 240\times 17}$. For the first- and second-order filters, 17 postfiltered images are averaged over either the slow-time or the frame-time axes to take full advantage of all echo data. The third-order filter first decomposes the entire data array before projecting onto the appropriate subspace. The entire echo-data array influences each image displayed in Fig. 9. In each case, we selected filter parameters that provided the clearest visualization of RBC movement. From one set of recorded echo data, we can see the effects of filter order and data-array axis (eigenbasis) on the ability to visualize fast or slow-flow patterns in normal and ischemic hindlimbs. In particular, compare the noise levels in the third-order filter results with the first- and second-order results. A noticeable contrast improvement is observed.

The full impact of using 3-D data may be appreciated when we threshold and color code the power signals before overlaying them on the B-mode image (Fig. 10) as is traditionally displayed for clinical applications. We use a blue color map to display the slow-time-axis power (arterial flows) seen in Fig. 9(E) and (F) and a red color map to display the frame-time-axis power (blood perfusion) from Fig. 9(K) and (L). Colored PD images are displayed in the third row of Fig. 10. The inset shows that 160-μm-dia vessels are clearly resolved.

The first and second rows of Fig. 10 display FIR-filtered PD images, and the third row shows HOSVD-filtered images. All are computed from the same echo-data array. We applied a fixed 25-Hz high-pass FIR filter in Fig. 10(A) and (B) and a 150-Hz high-pass FIR filter in Fig. 10(C) and (D). While surface vessels and bone artifacts can be seen in the 25-Hz FIR-filtered and the HOSVD images of Fig. 10, only HOSVD images show slow flow within the interior vessels

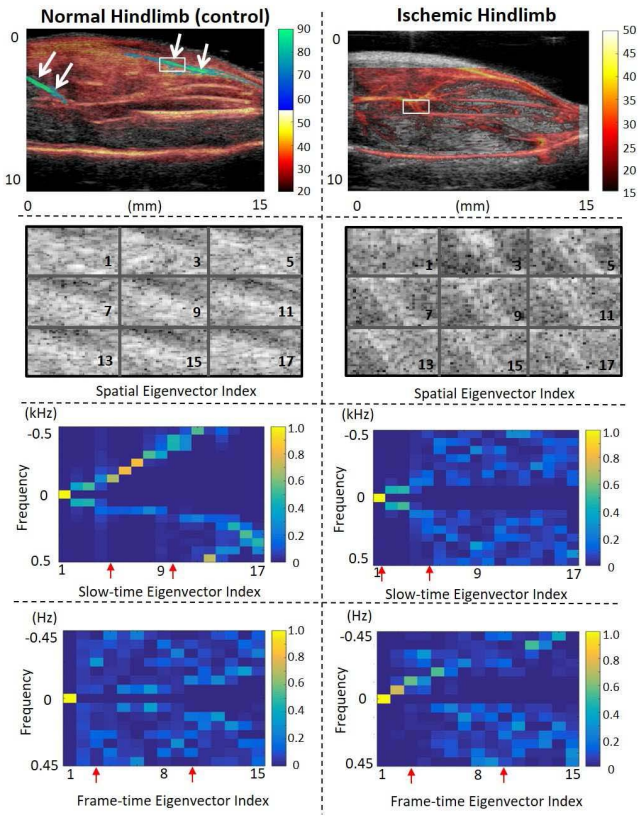

Fig. 11. Two columns illustrate analyses of data within local regions of three images. Top row shows the adaptive HOSVD images of normal and ischemic hindlimbs. White arrows indicate arterial flows, and boxes indicate analysis regions that include a vessel. The second row shows 9 of the first 18 spatial eigenvectors, some showing linear shapes similar to vessels seen in top-row images. Third and fourth rows show the power spectrum of slow-time and frame-time eigenvectors, respectively. The vertical axis is temporal frequency with the origin at the center, and the horizontal axis indicates eigenvectors along the corresponding axes, of which there are 17. Each column of the four spectral images is the absolute-square Fourier transform of the corresponding eigenvector. Eigenvectors between the red arrows were passed by the HOSVD filter for the images displayed in this report. Eigenvectors outside these ranges were removed by the filter.

of the ischemic hindlimb and uniformly perfused muscle in proximal regions of healthy controls. Sensitivity is reduced in distal muscle regions of all images as sound attenuation reduces SNCR.

IV. Discussion

These preliminary data suggest that the proposed changes in acquisition and filtering can greatly increase the sensitivity of ultrasonic power-Doppler perfusion imaging without contrast enhancement. The HOSVD filter allows us to separate fast and slow flows that we indicate with blue and red color maps in Fig. 10 (arrows in top row of Fig. 11 also indicate arterial flows). We were fortunate to capture a portion of the femoral artery in the ischemic image. This ligated vessel appears prominently in the perfusion image, because it is weakly fed from collateral vessels. Also, at 24 MHz, the ischemic hindlimb perfusion image inset in Fig. 10(E) clearly displays vessels with diameter smaller than 200 μm. These small vessels are less visible in the control hindlimb [Fig. 10(F)] where surrounding capillary perfusion reduces small-vessel contrast (not shown).

Baseline perfusion, which is 17 mL/min/100 g in the normal hindlimb [20], falls to 60%–70% of that value following femoral ligation [19]. Consequently, a 5–10 g hindlimb muscle has normal capillary flow in the range of 1–3 mL/min. A key element of successful HOSVD filtering is selection of the clutter and blood subspaces within core tensor, $\mathcal{G}$. The standard selection method is based on eigenvalue information and echogenic properties of the sources as mentioned in Section II-C. Since there are only a few prominent elements in $\mathcal{G}$, we now just try various filter ranges and inspect the resulting PD images to determine the "best" filter parameters. The following techniques using eigenvector information could guide a more objective and automated partitioning of $\mathcal{G}$.

The top-left PD image in Fig. 11 represents a different normal mouse hindlimb. Here, we see two segments of arterial flow as indicated by arrows and the blue–green color. On the right, we reproduce the ischemic hindlimb image from Fig. 10 that displays no fast blood flow patterns. In both images, we box a region of interest that includes directed vascular flows away from the transducer; on the left, flow velocity is in the range 2–15 mm/s and on the right, the flow velocity is in the range ± 0.2 mm/s.

In the second row of Fig. 11, we display the first nine odd spatial eigenvectors as gray scale images. These are taken from data in the boxed regions in the above-mentioned figures. The absolute values of elements in each spatial eigenvector are reshaped back into the shapes of the 2-D image patches. Looking closely, we see the linear shape of the vessel within each eigenvector that is similar to that in the above-mentioned boxed image region, except for the first eigenvector. The uniformity of spatial eigenvector 1 suggests that it is dominated by clutter, while the appearance of a vessel-like structure in the other eigenvectors suggests that they are influenced by directional blood flow in the vessel. For this reason, we eliminate at least the first spatial eigenmode through HOSVD filtering.

Images of the slow-time eigenvector spectra (third row in Fig. 11) and frame-time eigenvector spectra (fourth row) further reveal information about blood flow. In the first eigenvector spectrum (leftmost column of the spectral images), the only nonzero value is at zero frequency; consequently, the first eigenvector offers no information about movement and should be discarded. The linear spectral pattern in the normal hindlimb slow-time spectral image between eigenvectors 5 and 10 [third row in Fig. 11 (left)] suggests a strong signal is present for fast directed blood flow. Because this flow is away from the transducer, the linear pattern appears along the negative-frequency axis, which shows that there is directional flow information available. Notice that the spectrum shows evidence of aliasing as the linear structure wraps from negative to positive frequencies at eigenvector 13. There is no linear spectral pattern for the normal hindlimb image in the corresponding frame-time spectrum [fourth row in Fig. 11 (left)] as expected for the slow, disorganized RBC movement associated with capillary perfusion. The red arrows

along the abscissa indicate the upper and lower bounds on the eigenvector passband set for HOSVD filtering.

There is also an asymmetric linear spectral pattern in the ischemic hindlimb image between eigenvectors 3 and 9 in the frame-time spectrum [fourth row in Fig. 11 (right)]. This corresponds to the relatively slow but downward-directed flow within the large vessel in the ischemic tissue. We know that it is slow flow, because it is found in the frame-time spectrum and the linear pattern indicates that the flow is directed. Conversely, the slow-time eigenvector spectrum for the ischemic leg [third row in Fig. 11 (right)] is symmetric and diffuse, indicating no directed fast flow in this region.

Future work includes imaging at lower transmission frequencies and higher frame-time rates to assess clinical utility in human subjects. The low frame rate used for the murine model is unlikely to span the wider range of perfusion velocities found in human tissue.

V. Conclusion

In this paper, we found that expanding the dimension of the acquired echo-data array and then strategically reducing the data dimension using adaptive HOSVD filters lead to images that suggest improved perfusion sensitivity. At this point in development, the method offers images of signal power that describes relative flow and perfusion patterns.

HOSVD filtering appears to enhance the distinct information provided by each axis of the 3-D data array, enabling the visualization of blood components of the echo signal while effectively suppressing clutter and noise components. The addition of frame-time data as a separate array dimension appears to allow increased sensitivity to slower flows through a longer acquisition period without discarding fast blood flow echoes offered by the slow-time array axis. One 3-D acquisition processed via HOSVD effectively displays both blood components.

Although we apply power-Doppler processing here, we note that the eigenvector spectra seen in Fig. 11 contain information about the direction and spatial coherence of RBC movement. In principle, color-flow imaging is possible. We applied 24-MHz ultrasonic pulses to couple the method to the small mouse model which enabled submillimeter vessel diameter flows to be imaged with 5-mm tissue penetration.

The price paid for adding the frame-time axis in the echo-power estimator is that each PD frame requires more than 1 s worth of data acquisition. Since perfusion is normally steady or slowly varying, the long acquisition could be inconsequential depending on the application. The added sensitivity and lower noise justify the extra time and effort, especially when imaging stationary echo data that describe steady RBC movements, as for the application described in this report. Little effort has been made thus far to minimize the time required to compute one PD image frame, which now stands at 19.1 s.

Appendix

This Appendix briefly explains the outer-product notation used in Section II-C.3. The n-mode outer product of I_N-dimensional tensor $\boldsymbol{\mathcal{A}} \in \mathbb{C}^{I_1 \times I_2 \times \cdots \times I_{n-1} \times I_n \times I_{n+1} \times \cdots \times I_N}$ and matrix $\mathbf{Z} \in \mathbb{C}^{J_n \times I_n}$ is

$$\boldsymbol{\mathcal{D}} = \boldsymbol{\mathcal{A}} \times_n \mathbf{Z} \in \mathbb{C}^{I_1 \times \cdots \times I_{n-1} \times J_n \times I_{n+1} \times \cdots \times I_N}$$

where an element of tensor $\boldsymbol{\mathcal{D}}$ is

$$d_{i_1 \ldots i_{n-1} j_n i_{n+1} \ldots i_N} = \sum_{i_n=1}^{I_n} a_{i_1 \ldots i_N} z_{j_n i_n} \ .$$

The (ℓ_1, ℓ_2, ℓ_3)th element of $\boldsymbol{\mathcal{X}} \in \mathbb{C}^{N \times S \times K}$ is

$$x_{\ell_1,\ell_2,\ell_3} = \sum_{i_1=1}^{N} \sum_{i_2=1}^{S} \sum_{i_3=1}^{K} g_{i_1,i_2,i_3} u_{\ell_1,i_1} v_{\ell_2,i_2} w_{\ell_3,i_3}$$

which corresponds to a second line of (12).

References

[1] L. A. F. Ledoux, P. J. Brands, and A. P. G. Hoeks, "Reduction of the clutter component in Doppler ultrasound signals based on singular value decomposition: A simulation study," *Ultrason. Imag.*, vol. 19, no. 1, pp. 1–18, 1997.

[2] F. W. Mauldin, Jr., D. Lin, and J. A. Hossack, "The singular value filter: A general filter design strategy for PCA-based signal separation in medical ultrasound imaging," *IEEE Trans. Med. Imag.*, vol. 30, no. 11, pp. 1951–1964, Nov. 2011.

[3] C. Demené *et al.*, "Spatiotemporal clutter filtering of ultrafast ultrasound data highly increases Doppler and fUltrasound sensitivity," *IEEE Trans. Med. Imag.*, vol. 34, no. 11, pp. 2271–2285, Nov. 2015.

[4] V. Cantisani *et al.*, "Ambrosio, "Growing indications for CEUS: The kidney, testis, lymph nodes, thyroid, prostate, and small bowel," *Eur. J. Radiol.*, vol. 84, no. 9, pp. 1675–1684, 2015.

[5] W. Yang and P. J. Dempsey, "Diagnostic breast ultrasound: Current status and future directions," *Radiol. Clin. North Amer.*, vol. 45, no. 5, pp. 845–861, 2007.

[6] N. Oebisu *et al.*, "Contrast-enhanced color Doppler ultrasonography increases diagnostic accuracy for soft tissue tumors," *Oncol. Rep.*, vol. 32, no. 4, pp. 1654–1660, 2014.

[7] S. Bjærum, H. Torp, and K. Kristoffersen, "Clutter filter design for ultrasound color flow imaging," *IEEE Trans. Ultrason., Ferroelect., Freq. Control*, vol. 49, no. 2, pp. 204–216, Feb. 2002.

[8] L. Løvstakken, S. Bjærum, K. Kristoffersen, R. Haaverstad, and H. Torp, "Real-time adaptive clutter rejection filtering in color flow imaging using power method iterations," *IEEE Trans. Ultrason., Ferroelect., Freq. Control*, vol. 53, no. 9, pp. 1597–1608, Sep. 2006.

[9] A. C. H. Yu and L. Løvstakken, "Eigen-based clutter filter design for ultrasound color flow imaging: A review," *IEEE Trans. Ultrason., Ferroelect., Freq. Control*, vol. 57, no. 5, pp. 1096–1111, May 2010.

[10] L. De Lathauwer, B. De Moor, and J. Vandewalle, "A multilinear singular value decomposition," *SIAM J. Matrix Anal. Appl.*, vol. 21, no. 4, pp. 1253–1278, 2000.

[11] G. Bergqvist and E. G. Larsson, "The higher-order singular value decomposition: Theory and an application [lecture notes]," *IEEE Signal Process. Mag.*, vol. 27, no. 3, pp. 151–154, May 2010.

[12] H. Niiyama, N. F. Huang, M. D. Rollins, and J. P. Cooke, "Murine model of hindlimb ischemia," *J. Vis. Experim.*, no. 23, p. e1035, 2009.

[13] R. N. McDonough and A. D. Whalen, *Detection of Signals in Noise*, 2nd ed. San Diego, CA, USA: Academic, 1995.

[14] S. Bjærum, H. Torp, and K. Kristoffersen, "Clutter filters adapted to tissue motion in ultrasound color flow imaging," *IEEE Trans. Ultrason., Ferroelect., Freq. Control*, vol. 49, no. 6, pp. 693–704, Jun. 2002.

[15] Z.-P. Liang, "Spatiotemporal imaging with partially separable functions," in *Proc. IEEE Int. Symp. Biomed. Imag.*, Oct. 2007, pp. 181–182.

[16] D. Muti and S. Bourennane, "Multidimensional filtering based on a tensor approach," *Signal Process.*, vol. 85, no. 12, pp. 2338–2353, 2005.

[17] L. De Lathauwer, B. De Moor, and J. Vandewalle, "On the best rank-1 and rank-(R_1, R_2, ..., R_N) approximation of higher-order tensors," *SIAM J. Matrix Anal. Appl.*, vol. 21, no. 4, pp. 1324–1342, 2000.

[18] N. Vannieuwenhoven, R. Vandebril, and K. Meerbergen, "A new truncation strategy for the higher-order singular value decomposition," *SIAM J. Sci. Comput.*, vol. 34, no. 2, pp. A1027–A1052, 2012.
[19] J. Hua *et al.*, "Noninvasive imaging of angiogenesis with a ^{99m}Tc-labeled peptide targeted at $\alpha_v\beta_3$ integrin after murine hindlimb ischemia," *Circulation*, vol. 111, no. 24, pp. 3255–3260, 2005.
[20] D. Bertoldi, P. L. de Sousa, Y. Fromes, C. Wary, and P. G. Carlier, "Quantitative, dynamic and noninvasive determination of skeletal muscle perfusion in mouse leg by NMR arterial spin-labeled imaging," *Magn. Reson. Imag.*, vol. 26, no. 9, pp. 1259–1265, 2008.

MinWoo Kim, photograph and biography not available at the time of publication.

Craig K. Abbey, photograph and biography not available at the time of publication.

Jamila Hedhli, photograph and biography not available at the time of publication.

Lawrence W. Dobrucki, photograph and biography not available at the time of publication.

Michael F. Insana, (M'85–SM'06–F'12) photograph and biography not available at the time of publication.